Effect of low-frequency optical phonons on the thermal conductivity of 2*H* molybdenum disulfide

Zuo-Yuan Dong [1,2] Yan Zhou,[2] Xin-Qian Chen,[1] Wei-Jian Li,[2] Zi-Yu Cao,[2] Chen Luo,[1] Guo-Hua Zhong [3,4]
Qing Peng [3,5,*] Xing Wu,[1,†] and Xiao-Jia Chen[3,2,‡]

[1]*School of Communication and Electronic Engineering, East China Normal University, Shanghai 200241, China*
[2]*Center for High Pressure Science and Technology Advanced Research, Shanghai 201203, China*
[3]*School of Science, Harbin Institute of Technology, Shenzhen 518055, China*
[4]*Center for Photonics Information and Energy Materials, Shenzhen Institute of Advanced Technology,*
Chinese Academy of Sciences, Shenzhen 518055, China
[5]*State Key Laboratory of Nonlinear Mechanics, Institute of Mechanics, Chinese Academy of Sciences, Beijing 100190, China*

Phonon engineering is a novel and effective approach to tailor the thermal conductivity for the thermoelectric performance and heat dissipation. In general, the acoustic phonons rather than the optical phonons are dominant in heating carriers. Here we report an unprecedented large contribution, 47% overall, from the low-frequency optical phonons to the in-plane thermal conductivity in 2H molybdenum disulfide, revealed by low-wave-number high-pressure Raman technology assisted with first-principles calculations. The analysis of phonon dispersion curves and Grüneisen parameters of individual phonon modes reveals that the large contribution originates in a joint effect of the large group velocity of low-frequency optical phonons and their strong anharmonic effects. The joint effect is continuously maintained when pressure increases, up to 20 GPa. Our work provides new insights into the optical phonon transport, paving the way for the phonon engineering and thermal management.

I. INTRODUCTION

The thermal conductivity is a fundamental physical quantity to evaluate the heat transport performance of materials, playing an important role in the fields of thermoelectrics, electronics, thermal insulation, and heat management [1–3]. Phonons are the major carriers for heat transport in insulators and semiconductors. The thermal conductivity from phonon contributions in crystals is also called the lattice thermal conductivity. In thermoelectrics, for enhancing the figure of merit *zT* of thermoelectric materials, one effective approach is to suppress the lattice thermal conductivity since the electrons contribution is trivial [4,5]. In electronics, efficient heat dissipation is a prerequisite for ensuring the normal operation of the devices to avoid meltdown, which can be achieved by improving the lattice thermal conductivity [3]. Phonon-mediated intrinsically high thermal conductivity is the base in material design of anisotropic thermal conductors and real-world applications [6].

Heat transport needs both a medium (phonon or electrons) and channels (phonon bands or electron bands). For semiconductors, the thermal conductance contributed from electrons is negligible, for example, less than 0.01% in MoS_2 [7]. The carrier phonon has two categories of channels: acoustic and optic. The number of acoustic modes or channels is a constant three, while the optic channel has modes of $3N - 3$, where $3N$

is the degrees of freedom of the primitive cells of the system. For semiconductors and insulators, the lattice thermal conductivity receives predominant contributions not from optic phonons but from acoustic phonons. Despite the majority in number of channels, the optical phonons are always negligible due to their short lifetimes and low group velocities [8,9]. Utilizing the optic modes for phonon-mediated heat transport could open a new horizon of heat management. The ratio $\rho_o = \sigma_o/\sigma_a$ measures the contribution of optic phonons to the total lattice thermal conductance. Phonon-engineering for high ρ_o could revolutionize the heat management and heat harvesting.

It has been reported that in some cases, optical phonons can no longer be ignored in thermal transport. For example, theoretical calculations [10] indicate that the low-frequency optical phonon modes play a considerably important role in the thermal conductivity in β-Ga_2O_3. This is partially because the low-frequency optical branches have non-negligible group velocities compared with the acoustic ones. The optical phonon contribution can reach 46% in the two-dimensional (2D) material fluorinated diamane owing to the entanglement of optical phonons with the acoustic phonons, with the penalty of a dramatic (82%) drop in the thermal conductivity [11]. Experimental evidence of high ρ_o in bulk materials is still in elusive.

With the emergence of increasingly mature synthesis techniques, high-quality van der Waals solids with layered structures including transition-metal dichalcogenides (TMDCs) become promising candidates for applications in electronics, optoelectronics, and thermoelectrics [12,13]. TMDCs are typical anisotropic layered materials with van der

*pengqing@hit.edu.cn
†xwu@ee.ecnu.edu.cn
‡xjchen2@gmail.com

Waals interactions between layers. TMDCs have the formula of MX_2, where M stands for a transition-metal element, for example Mo, W, etc., and X refers to a chalcogen element (S, Se, or Te). Previous works on TMDCs show that the optical phonons possess large anharmonicity and herald the important role of optical phonons in thermal conductance [14–16]. The Grüneisen parameter is valuable to evaluate the strength of anharmonicity [17], and it is necessary to know the Grüneisen parameters of TMDCs. Experimentally, Raman spectroscopy is powerful in studying optical phonons, providing key information of phonon scattering and lattice dynamics [18]. The Grüneisen parameters for individual phonon modes can be computed from the pressure-dependent Raman spectroscopy [19–21]. Pressure dependence of the low-frequency optical phonon mode E_{2g}^2 in TMDCs (with the low wave numbers, such as 32, 25.4, and 23.7 cm^{-1} for MoS$_2$, MoSe$_2$, and WSe$_2$, respectively [22]) has been rarely studied [23,24]. The phonon dispersions of TMDCs [25] suggest that low-frequency optical phonons overlap with acoustic phonons, indicating the important role of these optical phonons for the thermal transport.

On the simulation side, the development of first-principles phonon calculations combining density-functional theory (DFT) and the Boltzmann transport equation (BTE) has rendered predictions of phonon transport properties more credible [1]. Through analyzing the phonon interaction dynamics, this method can provides the detailed explanations and reliable predictions of the performance of lattice thermal conductivity [26–29]. In addition, pressure can tune the phonon transport through lattice compression, and the behavior of phonons under pressure is always interesting [7,30,31]. So far, there is no systematic study of the individual optical phonon mode thermal conductivity from ambient to high pressures. Exploring the contributions of the low-frequency phonons at ambient pressure and high pressure as a function of temperature from both the experimental and theoretical sides is highly desired for the understanding of the thermal transport properties and the device developments based on these materials.

Taking MoS$_2$ as a prototype, we employ low-wave-number Raman technology to acquire its high-pressure Raman spectra (up to 20 GPa) assisted with a diamond-anvil cell (DAC). The mode-wide Grüneisen parameters of the optical phonon modes including the low-frequency E_{2g}^2 mode are obtained by combining the Raman data with the high-pressure structural data. The phonon dispersions and lattice thermal conductivity of MoS$_2$ as functions of pressure and temperature are explored by means of first-principles calculations conjugated with BTE. The contributions of high- and low-frequency optical phonons to the thermal conductivity are then discussed in detail. The implications of the results for the device developments and thermal managements are given.

II. METHODS

A. Experimental methods

A high-quality MoS$_2$ single crystal was produced by HQ Graphene. A $50 \times 50 \times 20$ μm^3 sample was used for high-pressure Raman-scattering measurements in a DAC with 500 μm culets. The advanced low-wave-number Raman technology was described in our previous works [15,19,20]. We used Ne as pressure-transmitting medium. The laser wavelength and power was 488 nm and 1 mW, respectively. The integral time was 120 s. A small ruby ball was used to calibrate the pressure in the sample chamber. The scattered light was initially focused on an 1800 g/mm grating, followed by recording with a 1024 pixel Princeton charge-coupled device.

For the transmission electron microscopy (TEM) characterizations, we used dispersant-assisted liquid-phase exfoliation to prepare single- and few-layer MoS$_2$. The TEM images were acquired using a FEI Themis-Z Double-corrected TEM operated at an accelerating voltage of 200 kV.

B. First-principles calculations

Our plane-wave *ab initio* DFT calculations are performed using the VASP program [32]. The exchange-correlation functional is the generalized gradient approximation (GGA) of Perdew, Burke, and Ernzerhof (PBE) [33]. The van der Waals interactions [34] are considered by the zero damping DFT-D3 method of Grimme [35] due to the compromise between computing power and accuracy. The plane-wave-basis cutoff every is 500 eV. The integral in reciprocal space is on the $18 \times 18 \times 4$ Monkhorst-Pack grids of k-point mesh. The crystal structures are optimized until the forces on the atoms are smaller than 0.001 eV/Å. The energy convergence criterion of the electronic relaxation in self-consistent field method is 10^{-6} eV for geometry relaxation. The phonon dispersions are computed using the finite displacement method with the PHONOPY code [36] on an $11 \times 11 \times 11$ k-grid with $5 \times 5 \times 3$ supercells. For accurate phonon calculations, we have used an energy cutoff of 500 eV and an energy convergence of 10^{-7} eV.

C. Phonon transport

The phonon transport is governed by the Boltzmann transport equation (BTE) where the lattice thermal conductivity can be obtained. A linearized version of the BTE is self-consistently solved using the ShengBTE code [37,38]. The lattice thermal conductivity κ_l at temperature T is given by [37,39]

$$\kappa_l^{\alpha\beta} = \frac{\hbar^2}{k_B T^2 N\Omega} \sum_{\lambda} f_0(f_0+1)(\omega_\lambda)^2 v_\lambda^\alpha v_\lambda^\beta \tau_\lambda, \qquad (1)$$

where Ω is the volume of the unit cell, N the number of k points, and f_0 is the Bose–Einstein statistics. The angular frequency of phonon mode λ is ω_λ. v_λ^α and v_λ^β denote the components of the group velocity. τ_λ is the self-consistent phonon lifetime. The phonon lifetime τ is inversely related to the scattering rate. The total scattering rate has two parts. One is the anharmonic scattering rate $1/\tau^{anh}$. The other is the isotope scattering rate $1/\tau^{iso}$. Therefore, the total phonon lifetime is calculated as $\frac{1}{\tau} = \frac{1}{\tau^{anh}} + \frac{1}{\tau^{iso}}$.

The anharmonic scattering rate takes into account only the three-phonon scattering processes, which include absorption processes and emission processes. Absorption processes indicate that two incident phonons combine into one ($\omega_\lambda + \omega_{\lambda'} = \omega_{\lambda''}$). Emission processes describe that one incident phonon
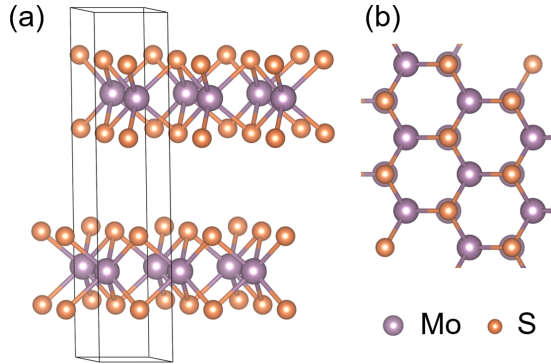
FIG. 1. The schematic diagrams of atomic configurations of bulk 2H phase MoS_2 (a) front view, and (b) top view in three unit cells. The large balls are Mo atoms and the small balls are S atoms.

splits into two phonons ($\omega_\lambda = \omega_{\lambda'} + \omega_{\lambda''}$). The quantities of three-phonon scattering rates therefore has two parts $\Gamma^{\pm}_{\lambda\lambda'\lambda''}$ for the absorption ($+$) and emission ($-$) processes, as described in the following two equations:

$$\Gamma^{+}_{\lambda\lambda'\lambda''} = \frac{\hbar\pi}{4}\frac{f_0' - f_0''}{\omega_\lambda\omega_{\lambda'}\omega_{\lambda''}}|V^{+}_{\lambda\lambda'\lambda''}|^2\delta(\omega_\lambda + \omega_{\lambda'} - \omega_{\lambda''}), \quad (2)$$

and

$$\Gamma^{-}_{\lambda\lambda'\lambda''} = \frac{\hbar\pi}{4}\frac{f_0' + f_0'' + 1}{\omega_\lambda\omega_{\lambda'}\omega_{\lambda''}}|V^{-}_{\lambda\lambda'\lambda''}|^2\delta(\omega_\lambda - \omega_{\lambda'} - \omega_{\lambda''}), \quad (3)$$

where $V^{\pm}_{\lambda\lambda'\lambda''}$ are the scattering matrix elements.

To evaluate the probabilities of anharmonic phonon scattering processes, a parameter W (also called "weighted phase space") is introduced as [27]

$$W^{\pm}_\lambda = \frac{1}{2N}\sum_{\lambda'p''}\left\{\begin{matrix}2(f_{\lambda'} - f_{\lambda''})\\f_{\lambda'} + f_{\lambda''} + 1\end{matrix}\right\}\frac{\delta(\omega_\lambda \pm \omega_{\lambda'} - \omega_{\lambda''})}{\omega_\lambda\omega_{\lambda'}\omega_{\lambda''}}, \quad (4)$$

.

The phonon transport properties mentioned above are determined by the lattice geometry and the interactions between atoms through the interatomic force constants (IFCs). The data of IFCs can be obtained from DFT calculations. The harmonic second-order IFCs are calculated by using $5 \times 5 \times 3$ supercells with a $2 \times 2 \times 2$ k grid. Considering the computational costs, the third-order IFCs calculations are performed on gamma-point only using $5 \times 5 \times 2$ supercells with seven nearest-neighbor interactions.

III. RESULTS AND DISCUSSION

A. Electronic structural properties

Among the diverse polytypes of bulk crystal MoS_2, the 2H phase is the most popular and studied in electronic devices [40]. Therefore, the 2H-MoS_2 is the focus of this study. Figure 1 exhibits the atomic structure of 2H-MoS_2. Crystalline 2H-MoS_2 has hexagonal symmetry. There are two S-Mo-S layers with a total of six atoms per unit cell. It is a semiconductor with covalent bonds between S and Mo within basal planes. On the contrary, the layers are connected by weak van der Waals force. The lattice parameters from our DFT results are 3.16 and 12.33 Å for the a and c axes, respectively, which
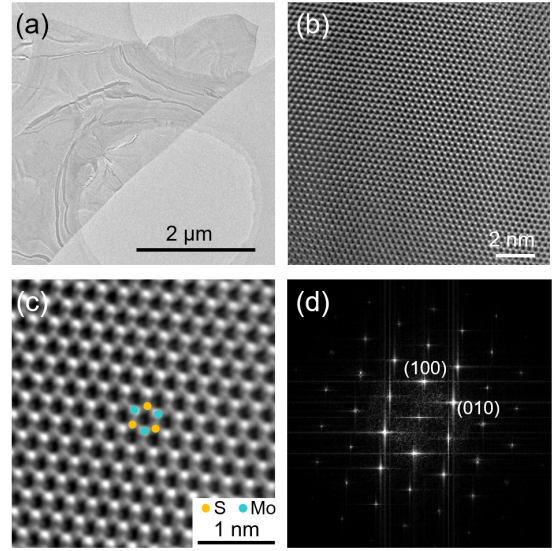

FIG. 2. Transmission electron microscopy (TEM) characterizations of single-crystal MoS_2 used in this experiment. (a) The TEM image of exfoliated MoS_2 sheet at a large scale. (b) The HRTEM image of the exfoliated MoS_2, with (c) enlarged view, and (d) fast Fourier transform (FFT) image. The scale bars and Mo, S elements are marked in the images.

is in good agreement with the previous theoretical [41] and experimental results [42].

B. Transmission electron microscopy characterization

The atomic structures of 2H MoS_2 have been characterized via transmission electron microscopy (TEM) technology, as displayed in Fig. 2 for the exfoliated MoS_2 sheets. A large scale in microns is shown in Fig. 2(a). To illustrate the atomic details, high-resolution transmission electron microscopy (HRTEM) images are presented in Fig. 2(b). An enlarged view is illustrated in Fig. 2(c). The fast Fourier transform (FFT) image is shown in Fig. 2(d). In the magnified view of Fig. 2(c), the honeycomb structure of MoS_2 can be clearly identified. The TEM images indicate that the MoS_2 crystal used in this experiment has a high quality in purity and perfection. Bulk 2H MoS_2 comprises 18 phonon vibration modes for the six-atom unit-cell crystal structure. There are three acoustic modes. The remaining 15 modes are optical modes. The irreducible representations of these 18 vibration modes at the Γ point in the Brillouin zone have irreducible representations such as $A_{1g} + E_{1g} + 2E_{2g} + 2A_{2u} + 2E_{1u} + E_{2u} + 2B_{2g} + B_{1u}$. Of these 18 modes, E_{2g}, E_{1g}, and A_{1g} are Raman active. At 2 K, the obtained E_{2g}^2, E_{2g}^1, and A_{1g} mode frequency is 34.6, 386.8, and 411.8 cm^{-1}, respectively, as displayed in Fig. 3. Our results are entirely consistent with previous experimental results and calculations [22].

C. Experimental mode Grüneisen parameters

The properties of phonons, especially the phonon anharmonicity, play an essential role in thermal transport. Related studies show that, for two components of the thermal conductivity of TMDCs, lattice thermal conductivity is dominant.
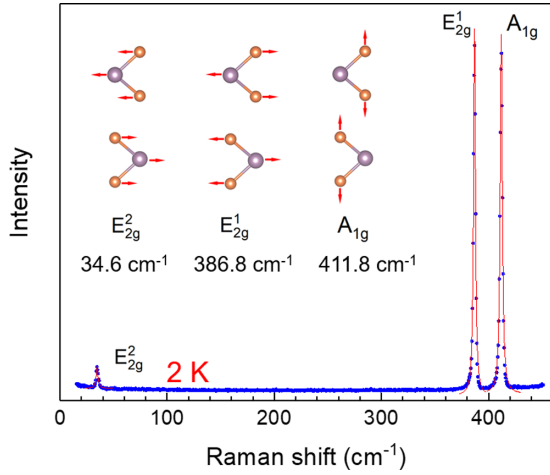
FIG. 3. The Raman spectrum of 2H MoS$_2$ at 2 K. The peaks of Raman modes E_{2g}^2, E_{2g}^1, and A$_{1g}$ are fit using a Lorentz function, and the insets give the corresponding diagrams of vibration modes.

The electronic thermal conductivity only accounts for a small portion due to their poor electrical conductivity because of the electronic band-gap energies [12]. The strength of the phonon anharmonicity is in general assessed by the mode Grüneisen parameter. A larger Grüneisen parameter means a stronger anharmonicity. Consequently, the lattice thermal conductivity decreases [17]. The Grüneisen parameter is defined as $\gamma_i = -\frac{d(\ln \omega_i)}{d(\ln V)}$, which reflects the relationship between the change of the crystal volume and the phonon frequency ω_i shift. When the volume change is mainly caused by the hydrostatic pressure, the Grüneisen parameter γ_i can be expressed as [19–21,45]

$$\gamma_i = \frac{B_0}{\omega_i^0} \frac{d\omega_i}{dP},$$ (5)

where B_0 is the bulk modulus, ω_i^0 is the ith phonon frequency at ambient pressure and room temperature, and $d\omega_i/dP$ is the frequency derivative of pressure. To obtain $d\omega_i/dP$ for MoS$_2$, high-pressure Raman-scattering experiments are performed at pressures up to 25 GPa.

Figure 4(a) illustrates the evolution of Raman peaks with pressure. In the entire pressure range, the three initially observed Raman peaks E_{2g}^2, E_{2g}^1, and A$_{1g}$ always exist. Above 20 GPa, both E_{2g}^1 and E_{2g}^2 peaks split into two peaks, which means that the phase transition of MoS$_2$ goes from the 2H$_c$ phase to the 2H$_a$ phase through layer sliding [36,42]. For the 2H$_c$ phase below 20 GPa, the pressure-dependent E_{2g}^2, E_{2g}^1, and A$_{1g}$ Raman modes are extracted and plotted in Fig. 4(b). A general trend is that all the phonon frequencies shift up under compression without distinct deviations. The frequency of each phonon mode is further analyzed by fitting to a quadratic function of pressure as

$$\omega_i(P) = \omega_i^0 + \frac{d\omega_i}{dP} + \frac{d^2\omega_i}{dP^2}P^2.$$ (6)

The obtained values of $d\omega_i/dP$ are listed in Table I. The first-order pressure coefficients of E_{2g}^2, E_{2g}^1, and A$_{1g}$ are 2.88 $\pm$ 0.06, 1.85 $\pm$ 0.04, and 3.31 $\pm$ 0.04 cm^{-1}/GPa, respectively.
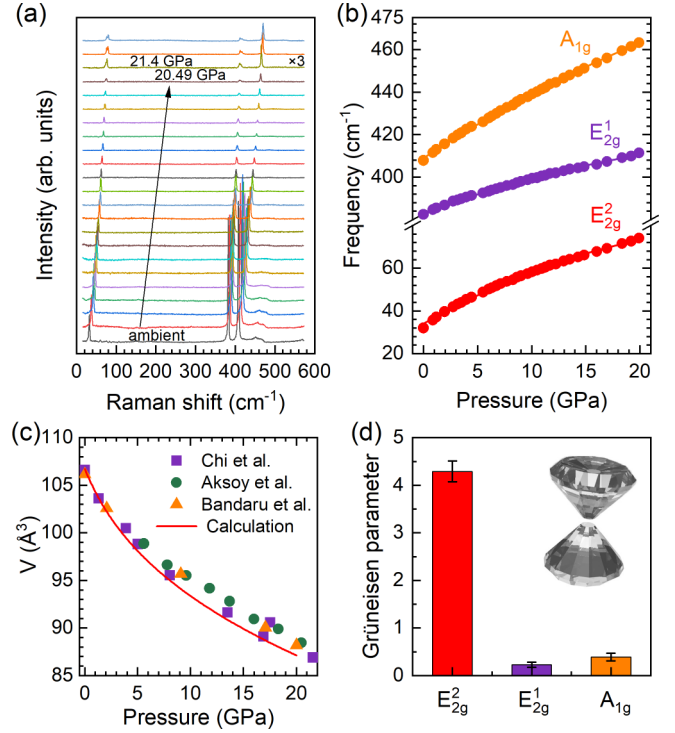

FIG. 4. (a) The pressure-dependent evolution of Raman spectra of MoS$_2$ from the ambient pressure to 25 GPa at room temperature. (b) The frequency of Raman-active phonon modes A$_{1g}$, E_{2g}^1, and E_{2g}^2 as a function of pressure. (c) The evolution of calculated crystal volume of MoS$_2$ with pressure (red line). Several typical experimental results are drawn in the subfigures [42–44]. (d) The obtained mode Grüneisen parameters of the three phonon modes. The inset is the sketch of the diamond anvil used in high-pressure Raman-scattering experiments.

The A$_{1g}$ mode is more sensitive to the change of pressure as compared with the E_{2g}^1 and E_{2g}^2 modes.

Bulk modulus $B_0 = -V_0 \frac{dP}{dV}$ is the elastic deformation relationship of the crystal volume with pressure [42], which is required for mode Grüneisen parameter. The bulk modulus can also be fit by using the Birch-Murnaghan equation [46]. The bulk modulus of MoS$_2$ is summarized in Table II. To obtain a reliable B_0 of MoS$_2$, we optimized the lattice parameters up to 20 GPa before phase transition.

Figure 4(c) shows the evolution of crystal volume with pressure, together with the experimental data. The unit-cell volume decreases from 106.7 to 87.1 Å^3 when the pressure increases from 0 to 20 GPa. The obtained bulk modulus is

TABLE I. Summary of the pressure coefficients of the phonon frequency ω, $d\omega_i/dP$ (in cm^{-1}/GPa) and $d^2\omega_i/dP^2$ (in cm^{-1}/GPa^2), as well as the mode Grüneisen parameters γ_i for three Raman modes of MoS$_2$.

	$d\omega_i/dP$	$d^2\omega_i/dP^2$	γ_i
E_{2g}^2	2.88 $\pm$ 0.057	-0.046 ± 0.002	4.29 $\pm$ 0.22
E_{2g}^1	1.85 $\pm$ 0.039	-0.025 ± 0.001	0.23 $\pm$ 0.054
A$_{1g}$	3.31 $\pm$ 0.044	-0.030 ± 0.002	0.39 $\pm$ 0.078

TABLE II. The calculated bulk modulus of MoS$_2$ compared with experimental results [42–44]. B_0 and B_0' are the bulk modulus and its pressure derivative at ambient pressure, respectively.

	B_0 (GPa)	B_0'
This work	40.6 ± 0.1	9.8 ± 0.04
Chi *et al.* [42]	47.65 ± 0.3	10.58 ± 0.08
Bandaru *et al.* [44]	70 ± 5	4.5
Aksoy *et al.* [43]	53.4 ± 1	9.2 ± 0.4

40.6 ± 0.1 GPa, which is the most consistent with the experimental result using the same transmitting medium Ne [42]. Combining B_0 of 47.65 ± 0.30 and $d\omega_i/dP$, the mode Grüneisen parameters of 2H MoS$_2$ are obtained as listed in Table I. They are also displayed in Fig. 4(d) for ease of comparison.

The values of the mode Grüneisen parameters are 4.29 ± 0.22, 0.23 ± 0.05, and 0.39 ± 0.08 for the E_{2g}^2, E_{2g}^1, and A$_{1g}$ modes, respectively. As shown in Fig. 4(d), it is obvious that the mode Grüneisen parameter of the low-frequency mode E_{2g}^2 is an order of magnitude larger than that of high-frequency modes (E_{2g}^1 and A$_{1g}$). The average Grüneisen parameter of these three modes is 2.49 ± 0.13, which is relatively large compared with other layered materials like boron nitride (BN) ($\langle \gamma \rangle = 0.7$) [47], and similar to black phosphorus ($\langle \gamma \rangle = 2.5$) [48].

D. Anisotropic phonon dispersions from the ambient to high pressures

Using the optimized unit-cell parameters, the phonon dispersions and the projected density of states (DOS) are calculated and illustrated in Fig. 5. The phonon dispersions exhibit the 18 phonon vibration branches and the Raman-active modes at the Γ point are marked. The calculated frequencies of the E_{2g}^2, E_{2g}^1, and A$_{1g}$ modes are 30.7, 382.8, and 410.3 cm^{-1}, respectively. Our results are slightly smaller than the experimental values obtained from Raman spectra (Fig. 3).
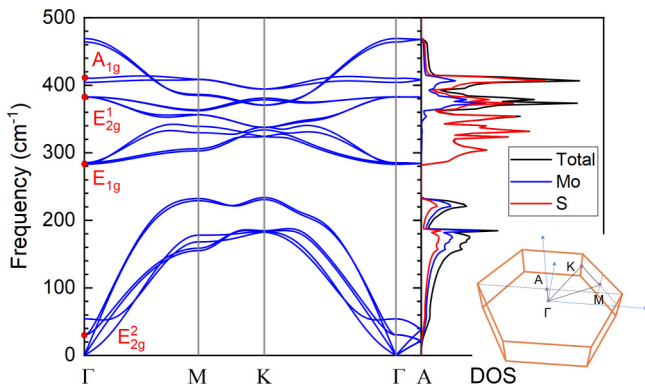

FIG. 5. The phonon dispersions and projected density of states (DOS) of MoS$_2$ at zero GPa. The vibration modes at Γ point are marked and the contribution of each atom is distinguished by color. The inset shows the path of the selected high-symmetry points in the Brillouin zone.
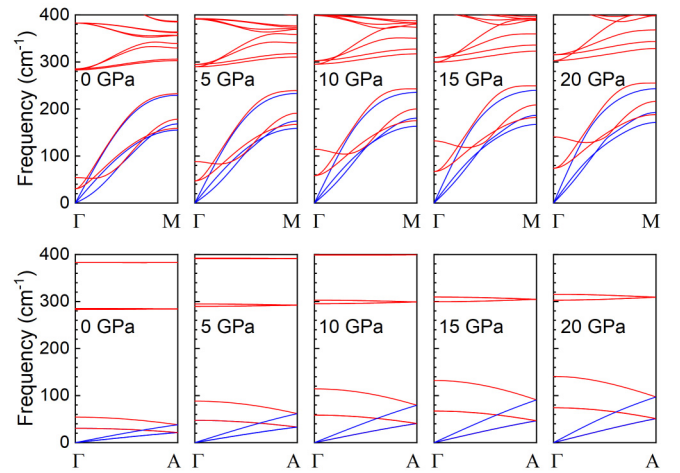

FIG. 6. The phonon dispersions of MoS$_2$ under pressure. The upper panels are along the Γ-M direction, and the bottom panels are along the Γ-A direction. The blue and red lines are intended to distinguish between the acoustic and optical branches. The corresponding pressure values are marked in the subfigures.

There is a band gap between 235 and 282 cm^{-1} in the phonon dispersion curves (Fig. 5). To facilitate the understanding of phonon properties, we denote the region above the phonon band gap as the high-frequency phonon region and that below the phonon band gap as the low-frequency phonon region. In the Brillouin zone, Γ-M (or Γ-K) refers to the direction along the in-plane and Γ-A means along the out-of-plane direction. In the low-frequency region, the difference between the two directions is the slope of the phonon dispersion curves or the phonon group velocities. The slopes of Γ-M and Γ-K are larger than that of Γ-A. This indicates that the phonon group velocity toward the a, b directions is greater than that toward the c direction.

The high-frequency optical phonons are relatively flat and do not contribute much to the phonon group velocity. The group velocity shows anisotropy in and out of plane. The phonon DOS shows that the high-frequency modes is mainly derived from the vibrations of the S atom. The contribution of Mo atom in the low-frequency region exceeds that of S atom because of the larger mass of Mo.

The high-pressure phonon dispersions are calculated as shown in Fig. 6 along Γ-M and Γ-A from 0 to 20 GPa. The acoustic branches and the optical branches are clearly distinguished by the red and blue lines. With the increment in pressure, all phonon vibration frequencies increase, predicting the continuous increase of thermal conductivity with pressure.

Phonon velocity is pressure dependent and nonisotropic. The slopes along the Γ-M direction do not change significantly with pressure. On the contrary, the slopes of the acoustic-phonon branches along the Γ-A direction have a large increase as the pressure rises. In addition, at all pressures, the low-frequency optical phonons exhibit unusual properties along Γ-M, reflected in two aspects: (1) The in-plane phonon group velocities of the low-frequency optical branches are significantly higher than that of the high-frequency ones. They are comparable to that of the acoustic ones. (2) The low-frequency optical modes entangle with the
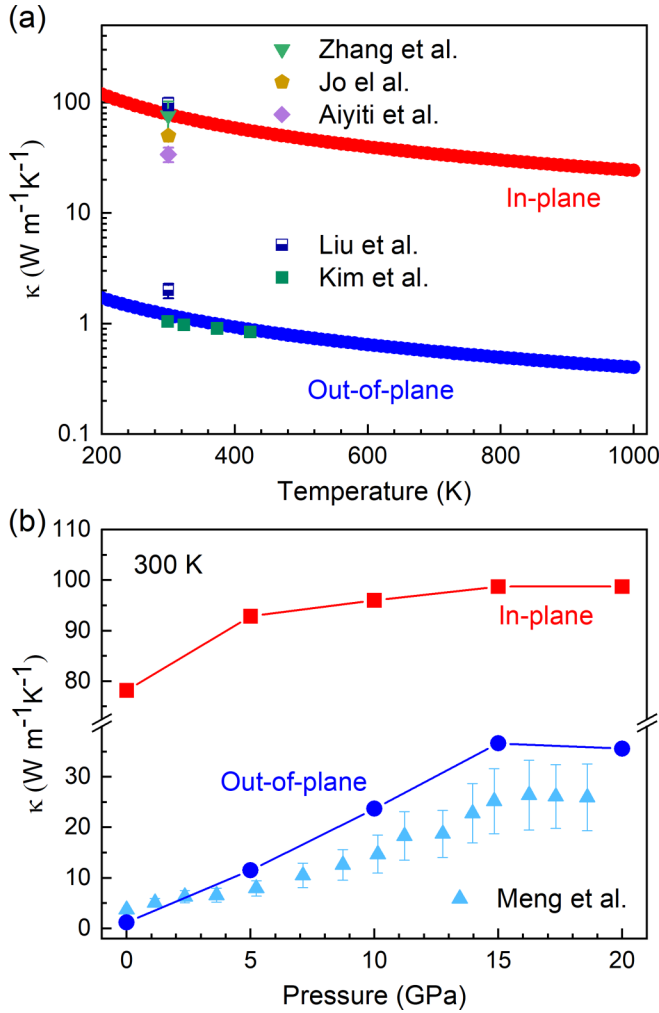
FIG. 7. (a) The lattice thermal conductivity of MoS_2 along the in-plane and out-of-plane directions at the temperature range from 200 to 1000 K. Previous experimental data are plotted for comparison [49–53]. (b) The high-pressure thermal conductivity along the in-plane and out-of-plane directions up to 20 GPa at 300 K. The experimental results of Meng *et al.* are drawn with triangular symbols [7].

acoustic branches. In contrast, the high-frequency branches have a significant gap. These factors indicate that the effect of the low-frequency optical phonons may be important in controlling the thermal transport of MoS_2.

E. Mode-wide thermal conductivity

The phonon behavior determines many physical properties, including the lattice thermal conductivity. We have theoretically predicted the lattice thermal conductivity of 2H MoS_2 accordingly. Figure 7(a) exhibits the temperature dependence of the lattice thermal conductivities along two different directions, the in-plane (κ_{xx}) and out-of-plane (κ_{zz}) directions. The temperature ranges from 200 to 1000 K. The thermal conductivity shows a large anisotropy, which is 78.2 W m^{-1} K^{-1} for the in-plane direction, but only 1.2 W m^{-1} K^{-1} along the out-of-plane direction at 300 K. These values are consistent with previous experiments and calculations [39,49–53].

It is worth mentioning that our calculated results are larger than the experimental values. This discrepancy comes from the fact that our numerical model is ideal without any defects, as opposed to that in specimens in experiments. The presence of defects enhances the phonon scattering and reduces the mean-free path [54], resulting in the lower thermal conductivity in experiment than in the ideal model in computation. Our results also agree with previous computational results [55,56].

The thermal conductivity of 2H MoS_2 decreases monotonically with respect to an increase in temperature, mainly owing to the Umklapp phonon scattering. As a widely used semiconductor, MoS_2 has a relatively small thermal conductivity, compared with Si of 142 W m^{-1} K^{-1}, BN of 760 W m^{-1} K^{-1} [57], and SiC of 360 W m^{-1} K^{-1} [47]. The small thermal conductivity greatly hinders commercial applications of MoS_2 as semiconductor devices due to accumulated heating. To overcome this shortcoming, previous works [7] demonstrated a significant enhancement in out-of-plane thermal conductivity of MoS_2 with pressure. Our theoretical results manifested two key factors: (1) both the in-plane and out-of-plane thermal conductivities increase with pressure; and (2) such pressure enhancement is only up to a pressure about 20 GPa, as shown in Fig. 7(b).

At room temperature, the in-plane thermal conductivity κ_{xx} increases from 78.2 to 98.7 W m^{-1} K^{-1} when the temperature increases from 0 to 20 GPa. The initial increment is more considerable, then eventually tends to saturation. The same trend is observed in the out-of-plane thermal conductivity κ_{zz}, which increases from 1.2 to 35.5 W m^{-1} K^{-1} in the same range of pressure, with a more significant increase up to 15 GPa, then saturates. The origin of the anisotropy of the thermal conductivity is the anisotropy of group velocity discussed above. In addition, the out-of-plane thermal conductivity is more sensitive to the pressure increment than the in-plane counterpart. This is because the pressure has little effect on the group velocity along Γ-M, but has a significant enhancement in the group velocity along Γ-A, as shown in Fig. 6.

Subsequently, we calculated the mode-wide contribution to the thermal conductivity. The individual mode along the in-plane and out-of-plane directions of MoS_2 at 300 K are shown in Figs. 8(a) and 8(b) for their contributions. 1-3 modes (blue bars) are the acoustic modes, 4-6 (red bars) refer to the low-frequency modes, and the remaining (purple bars) are the high-frequency optical modes. From Fig. 8(a), one can see that the contribution of the low-frequency optical branches exceed 47%, which can be comparable to that of the acoustic branches (50.7%). Their contributions are much more than those of the high-frequency branches (2.2%). The cumulative thermal conductivity are displayed in the inset of Fig. 8(a) as a function of frequency. It suggests that the main contribution is from 100–200 cm^{-1} phonons. Such a range of phonons frequencies is coincident with the overlap region of the acoustic and low-frequency optical branches.

Different to the in-plane behavior, the out-of-plane thermal conductivity receives contributions mainly from the acoustic phonons, which exceed 69.8%, while the low-frequency optical branches only account for 17.9%, as illustrated in Fig. 8(b). This may be explained from the phonon dispersion relationship. Low-frequency optical phonons have a higher group velocity during the in-plane transport. They are
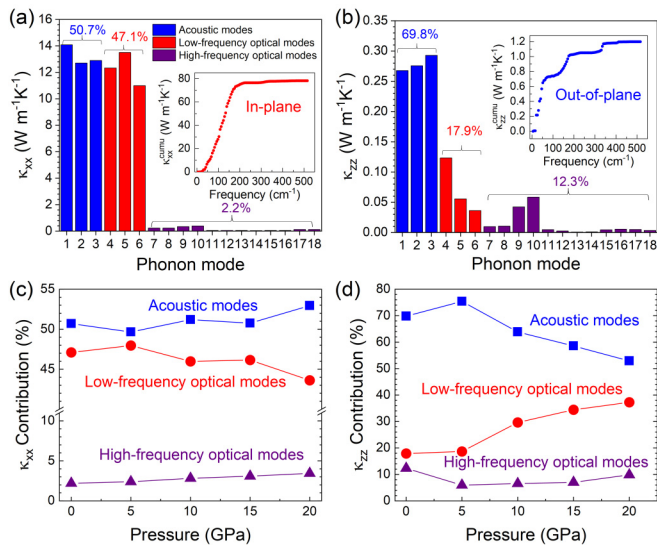
FIG. 8. The contribution of the phonon mode to the thermal conductivity of MoS$_2$ at ambient and high pressures at 300 K. (a) The contribution along the in-plane direction. 1-3 modes refer to the acoustic modes, 4-6 are the low-frequency optical modes, and others are the high-frequency modes. The inset is the cumulative thermal conductivity along the in-plane direction. (b) The contribution along the out-of-plane direction. The inset is the cumulative thermal conductivity along the out-of-plane direction. (c), (d) The phonon mode contribution as a function of pressure along the in-plane and out-of-plane directions, respectively.

FIG. 9. (a) Group velocity, (b) phonon lifetimes, (c) frequency-dependent mode Grüneisen parameters, and (d) weighted phase space of MoS$_2$ at 300 K.

complicatedly interwoven with acoustic phonons. This interweaving enlarges phonon scattering due to additional channels, leading to the enhancement of the contribution of the optical phonons in thermal transport.

As the pressure is increased, for in-plane thermal conductivity κ_{xx}, the contribution of the low-frequency optical phonons decreases [Fig. 8(c)]. This contribution increases for κ_{zz}, as shown in Fig. 8(d). The reduced contribution in κ_{xx} is due to the weakening of the coupling between the acoustic and optical branches along Γ-M under pressure (see Fig. 6). The rising contribution in κ_{zz} mainly depends on the significant enhancement of out-of-plane phonon velocity with pressure.

To further understand the thermal conductivity and the underlying mechanism of the contribution of low-frequency optical phonons in MoS$_2$, we have analyzed the frequency-dependent phonon group velocities, lifetimes, and Grüneisen parameters, shown in Figs. 9(a)–9(c). The frequency dependence of the group velocities are displayed in different colors to distinguish the acoustic, low-frequency, and high-frequency optical phonons in Fig. 9(a). The low-frequency optical phonons have very large group velocities, which even exceed the contribution from the acoustic ones. The phonon lifetimes of the low-frequency optical phonons are comparable to those of the acoustic ones, which is much longer than those of high-frequency phonons, as shown in Fig. 9(b). The two synergistic factors make the low-frequency optical phonons unprecedented large contribution to the thermal conductivity.
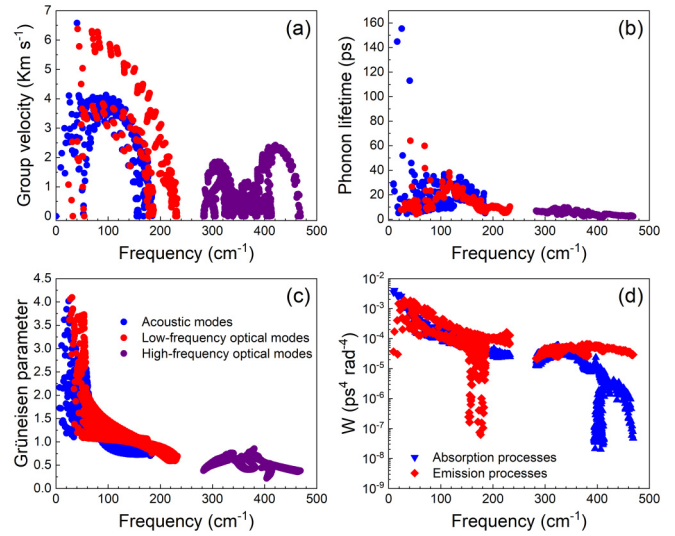
Figure 9(c) displays the mode Grüneisen parameters with frequency. The values of low-frequency phonons are much larger than those of the high-frequency ones, which also agrees with our experiments. The large mode Grüneisen parameters are related to the anharmonic scattering of phonons. In addition, according to the previous work, the weighted phase space (W) can evaluate the anharmonicity [27]. The results of our weighted phase space values are plotted in Fig. 9(d). The blue (red) curve exhibits the absorption (emission) processes in the three-phonon scattering process. The anharmonicity of the low-frequency phonons is stronger, consistent with the large Grüneisen parameters compared with that of the high-frequency ones.

It is worth pointing out that our results have manifested that, besides the acoustic phonons, the optical phonons play a non-negligible role in the thermal transport of MoS$_2$. If the optical phonons are not considered, the phonon-phonon scattering will reduce due to the reduction of complicity, which will undoubtedly overestimate the thermal conductivity. The combined effect of optical-phonon and acoustic-phonon scattering suppresses the thermal conductivity.

The discovered large contribution from the low-frequency optical phonon modes to the total lattice thermal conductivity in MoS$_2$ is important in understanding the thermal transport, not only in the 2H MoS$_2$ system itself, but also for the device developments and material design. Currently, MoS$_2$ is being examined in the applications in quantum information and quantum computing. It finds potential technological applications as nanoscale drum for quantum information storage [58], as well as energy storage [59]. Meanwhile, it may also be used to transmit quantum information through propagating phonons coupled to artificial atoms [60]. The significant contributions of the low-frequency phonon mode to the thermal conductivity, and strong anisotropy of the thermal transport upon lattice compression should be considered for the phonon engineering, material design, and device developments.

IV. CONCLUSIONS

We have investigated the mode-wide thermal conductivity of the single-crystal 2H phase MoS_2 under high pressures as a model material of transition-metal dichalcogenides by using a combined approach of experiment, computations, and theoretical analysis. Various experimental techniques are employed including low-wave-number Raman experiments, diamond-anvil cell high pressure, and transmission electron microscopy characterization. The phonon dispersion curves are obtained through the first-principles calculations. The thermal conductivity is predicted through the Boltzmann transport equation. We have revealed the unprecedented large contributions to the thermal conductivity from low-frequency phonon modes.

We have calculated the mode Grüneisen parameters of the E_{2g}^2, E_{2g}^1, and A_{1g} modes. We have observed that the Grüneisen parameter of the low-frequency optical mode E_{2g}^2 (below the phonon band gap) is an order of magnitude larger than those of the high-frequency modes (above the phonon band gap). First-principles calculations reveal that the low-frequency optical phonons have a large contribution ($\rho_o = 47\%$) to the in-plane thermal conductivity, which is comparable to the contribution from the acoustic phonons and continuously maintains up to 20 GPa. This unprecedented large contribution from the low-frequency optical mode is due to the two unique characteristics of the low-frequency optical phonons: large group velocities and long lifetime, which are comparable to those of the acoustic counterparts. The strong anharmonic effect between the acoustic and optical phonons affects the contribution of thermal conductivity. Our work might be helpful in material design, phonon engineering, and heat management.

[1] X. Qian, J. Zhou, and G. Chen, Phonon-engineered extreme thermal conductivity materials, Nat. Mater. **20**, 1188 (2021).

[2] G. J. Snyder and E. S. Toberer, Complex thermoelectric materials, Nat. Mater. **7**, 105 (2008).

[3] X. Gu, Y. Wei, X. Yin, B. Li, and R. Yang, Colloquium: phononic thermal properties of two-dimensional materials, Rev. Mod. Phys. **90**, 041002 (2018).

[4] C. Fu, H. Wu, Y. Liu, J. He, X. Zhao, and T. Zhu, Enhancing the figure of merit of heavy-band thermoelectric materials through hierarchical phonon scattering, Adv. Sci. (Weinheim, Ger.) **3**, 1600035 (2016).

[5] W. Ren, Q. Song, H. Zhu, J. Mao, L. You, G. A. Gamage, J. Zhou, T. Zhou, J. Jiang, C. Wang, J. Luo, J. Wu, Z. Wang, G. Chen, and Z. Ren, Intermediate-level doping strategy to simultaneously optimize power factor and phonon thermal conductivity for improving thermoelectric figure of merit, Mater. Today Phys. **15**, 100250 (2020).

[6] S. E. Kim, F. Mujid, A. Rai, F. Eriksson, J. Suh, P. Poddar, A. Ray, C. Park, E. Fransson, Y. Zhong, D. A. Muller, P. Erhart, D. G. Cahill, and J. Park, Extremely anisotropic van der Waals thermal conductors, Nature (London) **597**, 660 (2021).

[7] X. Meng, T. Pandey, J. Jeong, S. Fu, J. Yang, K. Chen, A. Singh, F. He, X. Xu, J. Zhou, W.-P. Hsieh, A. K. Singh, J.-F. Lin, and Y. Wang, Thermal Conductivity Enhancement in MoS_2 Under Extreme Strain, Phys. Rev. Lett. **122**, 155901 (2019).

[8] D. A. Broido, M. Malorny, G. Birner, N. Mingo, and D. A. Stewart, Intrinsic lattice thermal conductivity of semiconductors from first principles, Appl. Phys. Lett. **91**, 231922 (2007).

[9] D. P. Sellan, J. E. Turney, A. J. H. McGaughey, and C. H. Amon, Cross-plane phonon transport in thin films, J. Appl. Phys. **108**, 113524 (2010).

[10] Z. Yan and S. Kumar, Phonon mode contributions to thermal conductivity of pristine and defective β-Ga_2O_3, Phys. Chem. Chem. Phys. **20**, 29236 (2018).

[11] L. Zhu and T. Zhang, Suppressed thermal conductivity in fluorinated diamane: optical phonon dominant thermal transport, Appl. Phys. Lett. **115**, 151904 (2019).

[12] D. O. Lindroth and P. Erhart, Thermal transport in van der Waals solids from first-principles calculations, Phys. Rev. B **94**, 115205 (2016).

[13] Q. H. Wang, K. Kalantar-Zadeh, A. Kis, J. N. Coleman, and M. S. Strano, Electronics and optoelectronics of two-dimensional transition metal dichalcogenides, Nat. Nanotechnol. **7**, 699 (2012).

[14] Z.-Y. Cao and X.-J. Chen, Phonon scattering processes in molybdenum disulfide, Appl. Phys. Lett. **114**, 052102 (2019).

[15] Z.-Y. Dong, Y.-K. Peng, H. Yu, W.-J. Li, J.-W. Hu, C. Luo, X. Wu, and X.-J. Chen, Role of optical phonons in bulk molybdenum diselenide thermal properties probed by advanced Raman spectroscopy, Phys. Status Solidi B **257**, 2000251 (2020).

[16] Y.-K. Peng, Z.-Y. Cao, L.-C. Chen, N. Dai, Y. Sun, and X.-J. Chen, Phonon anharmonicity of tungsten disulfide, J. Phys. Chem. C **123**, 25509 (2019).

[17] C. Chang and L.-D. Zhao, Anharmoncity and low thermal conductivity in thermoelectrics, Mater. Today Phys. **4**, 50 (2018).

[18] Z. Dong, H. Xu, F. Liang, C. Luo, C. Wang, Z.-Y. Cao, X.-J. Chen, J. Zhang, and X. Wu, Raman characterization on two-dimensional materials-based thermoelectricity, Molecules **24**, 88 (2019).

[19] H. Yu, G. Huang, Q. Peng, L.-C. Chen, H.-J. Pang, X.-Y. Qin, P.-F. Qiu, X. Shi, L.-D. Chen, and X.-J. Chen, A combined experiment and first-principles study on lattice dynamics of thermoelectric $CuInTe_2$, J. Alloys Compd. **822**, 153610 (2020).

[20] L.-C. Chen, Q. Peng, H. Yu, H.-J. Pang, B.-B. Jiang, L. Su, X. Shi, L.-D. Chen, and X.-J. Chen, Lattice dynamics of thermoelectric palladium sulfide, J. Alloys Compd. **798**, 484 (2019).

[21] H.-J. Pang, L.-C. Chen, Z.-Y. Cao, H. Yu, C.-G. Fu, T.-J. Zhu, A. F. Goncharov, and X.-J. Chen, Mode Grüneisen parameters

of an efficient thermoelectric half-Heusler, J. Appl. Phys. **124**, 195107 (2018).

[22] S. V. Bhatt, M. P. Deshpande, V. Sathe, R. Rao, and S. H. Chaki, Raman spectroscopic investigations on transition-metal dichalcogenides MX_2 ($M =$ Mo, W; $X =$ S, Se) at high pressures and low temperature: Raman spectroscopic investigations on MX_2, J. Raman Spectrosc. **45**, 971 (2014).

[23] M. Yang, X. Cheng, Y. Li, Y. Ren, M. Liu, and Z. Qi, Anharmonicity of monolayer MoS_2, $MoSe_2$, and WSe_2: A Raman study under high pressure and elevated temperature, Appl. Phys. Lett. **110**, 093108 (2017).

[24] D. J. Late, S. N. Shirodkar, U. V. Waghmare, V. P. Dravid, and C. N. R. Rao, Thermal expansion, anharmonicity and temperature-dependent Raman spectra of single- and few-layer $MoSe_2$ and WSe_2, ChemPhysChem **15**, 1592 (2014).

[25] H. Tornatzky, R. Gillen, H. Uchiyama, and J. Maultzsch, Phonon dispersion in MoS_2, Phys. Rev. B **99**, 144309 (2019).

[26] J. Yu, J. Zhou, X. Wan, and Q. Li, High intrinsic lattice thermal conductivity in monolayer $MoSi_2N_4$, New J. Phys. **23**, 033005 (2021).

[27] W. Li and N. Mingo, Ultralow lattice thermal conductivity of the fully filled skutterudite $YbFe_4Sb_{12}$ due to the flat avoided-crossing filler modes, Phys. Rev. B **91**, 144304 (2015).

[28] S.-D. Guo and A.-X. Zhang, Phonon transport in Na_2He at high pressure from a first-principles study, Appl. Phys. Lett. **110**, 172104 (2017).

[29] H.-Y. Song, X.-J. Ge, M.-Y. Shang, J. Zhang, and J.-T. Lü, Intrinsically low thermal conductivity of bismuth oxychalcogenides originating from interlayer coupling, Phys. Chem. Chem. Phys. **21**, 18259 (2019).

[30] Y. Zhou, Z.-Y. Dong, W.-P. Hsieh, A. F. Goncharov, and X.-J. Chen, Thermal conductivity of materials under pressure, Nat. Rev. Phys. (2022).

[31] H.-J. Pang, L.-C. Chen, H. Yu, P.-F. Qiu, G.-H. Zhong, Q. Peng, and X.-J. Chen, Hybridization-driven strong anharmonicity in Yb-filled skutterudites, Phys. Rev. B **105**, 094115 (2022).

[32] G. Kresse and J. Furthmüller, Efficient iterative schemes for *ab initio* total-energy calculations using a plane-wave basis set, Phys. Rev. B **54**, 11169 (1996).

[33] J. P. Perdew, K. Burke, and M. Ernzerhof, Generalized Gradient Approximation Made Simple, Phys. Rev. Lett. **77**, 3865 (1996).

[34] Q. Peng, G. Wang, G.-R. Liu, and S. De, Van der Waals density functional theory vdw-dfq for semihard materials, Crystals **9**, 243 (2019).

[35] S. Grimme, J. Antony, S. Ehrlich, and H. Krieg, A consistent and accurate *ab initio* parametrization of density functional dispersion correction (DFT-D) for the 94 elements H-Pu, J. Chem. Phys. **132**, 154104 (2010).

[36] A. Togo and I. Tanaka, First principles phonon calculations in materials science, Scr. Mater. **108**, 1 (2015).

[37] W. Li, J. Carrete, N. A. Katcho, and N. Mingo, ShengBTE: A solver of the Boltzmann transport equation for phonons, Comput. Phys. Commun. **185**, 1747 (2014).

[38] W. Li, N. Mingo, L. Lindsay, D. A. Broido, D. A. Stewart, and N. A. Katcho, Thermal conductivity of diamond nanowires from first principles, Phys. Rev. B **85**, 195436 (2012).

[39] A. N. Gandi and U. Schwingenschlögl, Thermal conductivity of bulk and monolayer MoS_2, Europhys. Lett. **113**, 36002 (2016).

[40] S. Manzeli, D. Ovchinnikov, D. Pasquier, O. V. Yazyev, and A. Kis, 2D transition metal dichalcogenides, Nat. Rev. Mater. **2**, 17033 (2017).

[41] A. Molina-Sánchez, K. Hummer, and L. Wirtz, Vibrational and optical properties of MoS_2: from monolayer to bulk, Surf. Sci. Rep. **70**, 554 (2015).

[42] Z.-H. Chi, X.-M. Zhao, H. Zhang, A. F. Goncharov, S. S. Lobanov, T. Kagayama, M. Sakata, and X.-J. Chen, Pressure-Induced Metallization of Molybdenum Disulfide, Phys. Rev. Lett. **113**, 036802 (2014).

[43] R. Aksoy, Y. Ma, E. Selvi, M. C. Chyu, A. Ertas, and A. White, X-ray diffraction study of molybdenum disulfide to 38.8 GPa, J. Phys. Chem. Solids **67**, 1914 (2006).

[44] N. Bandaru, R. S. Kumar, D. Sneed, O. Tschauner, J. Baker, D. Antonio, S.-N. Luo, T. Hartmann, Y. Zhao, and R. Venkat, Effect of pressure and temperature on structural stability of MoS_2, J. Phys. Chem. C **118**, 3230 (2014).

[45] G. Lucazeau, Effect of pressure and temperature on Raman spectra of solids: Anharmonicity, J. Raman Spectrosc. **34**, 478 (2003).

[46] F. Rivadulla, M. Bañobre-López, C. X. Quintela, A. Piñeiro, V. Pardo, D. Baldomir, M. A. López-Quintela, J. Rivas, C. A. Ramos, H. Salva, J.-S. Zhou, and J. B. Goodenough, Reduction of the bulk modulus at high pressure in CrN, Nat. Mater. **8**, 947 (2009).

[47] C. Toher, J. J. Plata, O. Levy, M. de Jong, M. Asta, M. B. Nardelli, and S. Curtarolo, High-throughput computational screening of thermal conductivity, Debye temperature, and Grüneisen parameter using a quasiharmonic Debye model, Phys. Rev. B **90**, 174107 (2014).

[48] Y. Li, Z. Hu, S. Lin, S. K. Lai, W. Ji, and S. P. Lau, Giant anisotropic Raman response of encapsulated ultrathin black phosphorus by uniaxial strain, Adv. Funct. Mater. **27**, 1600986 (2017).

[49] X. Zhang, D. Sun, Y. Li, G.-H. Lee, X. Cui, D. Chenet, Y. You, T. F. Heinz, and J. C. Hone, Measurement of lateral and interfacial thermal conductivity of single- and bilayer MoS_2 and $MoSe_2$ using refined optothermal Raman technique, ACS Appl. Mater. Interfaces **7**, 25923 (2015).

[50] I. Jo, M. T. Pettes, E. Ou, W. Wu, and L. Shi, Basal-plane thermal conductivity of few-layer molybdenum disulfide, Appl. Phys. Lett. **104**, 201902 (2014).

[51] A. Aiyiti, S. Hu, C. Wang, Q. Xi, Z. Cheng, M. Xia, Y. Ma, J. Wu, J. Guo, Q. Wang, J. Zhou, J. Chen, X. Xu, and B. Li, Thermal conductivity of suspended few-layer MoS_2, Nanoscale **10**, 2727 (2018).

[52] J. Liu, G.-M. Choi, and D. G. Cahill, Measurement of the anisotropic thermal conductivity of molybdenum disulfide by the time-resolved magneto-optic Kerr effect, J. Appl. Phys. **116**, 233107 (2014).

[53] J.-Y. Kim, S. M. Choi, W.-S. Seo, and W.-S. Cho, Thermal and electronic properties of exfoliated metal chalcogenides, Bull. Korean Chem. Soc. **31**, 3225 (2010).

[54] C. Lu, T. Yang, L. Niu, Q. Peng, K. Jin, M. L. Crespillo, G. Velisa, H. Xue, F. Zhang, P. Xiu, Y. Zhang, F. Gao, H. Bei, W. J. Weber, and L. Wang, Interstitial migration behavior and defect evolution in ion irradiated pure nickel and Ni-xFe binary alloys, J. Nucl. Mater. **509**, 237 (2018).

[55] X. Gu, B. Li, and R. Yang, Layer thickness-dependent phonon properties and thermal conductivity of MoS_2, J. Appl. Phys. **119**, 085106 (2016).

[56] X. Xu, J. Chen, and B. Li, Phonon thermal conduction in novel 2D materials, J. Phys.: Condens. Matter **28**, 483001 (2016).

[57] H. R. Shanks, P. D. Maycock, P. H. Sidles, and G. C. Danielson, Thermal conductivity of silicon from 300 to 1400 K, Phys. Rev. **130**, 1743 (1963).

[58] V. Singh, S. J. Bosman, B. H. Schneider, Y. M. Blanter, A. Castellanos-Gomez, and G. A. Steele, Optomechanical coupling between a multilayer graphene mechanical resonator and a superconducting microwave cavity, Nat. Nanotechnol. **9**, 820 (2014).

[59] Q. Peng and S. De, Outstanding mechanical properties of monolayer MoS_2 and its application in elastic energy storage, Phys. Chem. Chem. Phys. **15**, 19427 (2013).

[60] M. V. Gustafsson, T. Aref, A. F. Kockum, M. K. Ekström, G. Johansson, and P. Delsing, Propagating phonons coupled to an artificial atom, Science **346**, 207 (2014).